Investigating the Radar Response of Englacial Debris Entrained Basal Ice Units in East Antarctica Using Electromagnetic Forward Modeling

Steven Franke, Tamara Gerber, Craig Warren, Daniela Jansen, Olaf Eisen, and Dorthe Dahl-Jensen

***Abstract*— Radio-echo sounding (RES) reveals patches of high backscatter in basal ice units, which represent distinct englacial features in the bottom parts of glaciers and ice sheets. Their material composition and physical properties are largely unknown due to their direct inaccessibility but could provide significant information on the physical state as well as on present and past processes at the ice-sheet base. Here, we investigate the material properties of basal ice units by comparing measured airborne radar data with synthetic radar responses generated using electromagnetic (EM) forward modeling. The observations were acquired at the onset of the Jutulstraumen Ice Stream in western Dronning Maud Land (DML) (East Antarctica) and show strong continuous near-basal reflections of up to 200-m thickness in the normally echo-free zone (EFZ). Based on our modeling, we suggest that these high-backscatter units are most likely composed of point reflectors with low dielectric properties, suggesting thick packages of englacial entrained debris. We further investigate the effects of entrained particle size, and concentration in combination with different dielectric properties, which provide useful information to constrain the material composition of radar-detected units of high backscatter. The capability and application of radar wave modeling in complex englacial environments is therefore a valuable tool to further constrain the composition of basal ice and the physical conditions at the ice base.**

***Index Terms*— Antarctic ice sheet, basal freeze-on, basal ice, electromagnetic (EM) forward modeling, gprMax, ice accretion, Jutulstraumen ice stream, radio-echo sounding (RES), sediment entrainment.**

Manuscript received 17 February 2023; revised 6 April 2023 and 8 May 2023; accepted 16 May 2023. Date of publication 19 May 2023; date of current version 7 June 2023. This work was supported in part by the NASA Operation IceBridge Grant through The University of Kansas under Grant NNX16AH54G; in part by the NSF under Grant ACI-1443054, Grant OPP-1739003, and Grant IIS-1838230; and in part by the Villum Investigator Project IceFlow under Grant 16572. The work of Steven Franke was supported in part by the German Academic Exchange Service (DAAD) Programme (Forschungsstipendien für promovierte Nachwuchswissenschaftlerinnen und-wissenschaftler; Kurzstipendien) and in part by the Walter Benjamin Programme of the Deutsche Forschungsgemeinschaft (DFG, German Research Foundation) under Project 506043073. *(Corresponding author: Steven Franke.)*

Steven Franke is with the Niels Bohr Institute, Physics of Ice, Climate and Earth, University of Copenhagen, 2200 Copenhagen, Denmark, and also with the Glaciology Section, Alfred-Wegener-Institut Helmholtz-Zentrum für Polar- und Meeresforschung (AWI), 27570 Bremerhaven, Germany (e-mail: steven.franke@awi.de).

Tamara Gerber is with the Niels Bohr Institute, Physics of Ice, Climate and Earth, University of Copenhagen, 2200 Copenhagen, Denmark (e-mail: tamara.gerber@nbi.ku.dk).

Craig Warren is with the Department of Mechanical and Construction Engineering, Northumbria University, NE1 8ST Newcastle, U.K. (e-mail: craig.warren@northumbria.ac.uk).

Daniela Jansen is with the Glaciology Section, Alfred-Wegener-Institut Helmholtz-Zentrum fur Polar- und Meeresforschung (AWI), 27570 Bremerhaven, Germany (e-mail: daniela.jansen@awi.de).

Olaf Eisen is with the Glaciology Section, Alfred-Wegener-Institut Helmholtz-Zentrum fur Polar- und Meeresforschung (AWI), 27570 Bremerhaven, Germany , and also with the Department of Geosciences, University of Bremen, 28359 Bremen, Germany (e-mail: olaf.eisen@awi.de).

Dorthe Dahl-Jensen is with the Niels Bohr Institute, Physics of Ice, Climate and Earth, University of Copenhagen, 2200 Copenhagen, Denmark, and also with the Centre for Earth Observation Science, University of Manitoba, Winnipeg, MB, Canada (e-mail: ddj@nbi.ku.dk).

Digital Object Identifier 10.1109/TGRS.2023.3277874

I. Introduction

THE future evolution of the Earth's climate is tightly interconnected with the behavior of the polar ice sheets. Processes acting at the ice-sheet surface are rather convenient to study, however, little is known about the processes at the ice-sheet base due to their direct inaccessibility. Aerogeophysical investigations, such as radio-echo sounding (RES), provide information about the layered internal age structure as well as some constraints about the ice–bed interface [1], [2], [3], [4] on larger spatial scales. In the bottom 10%–30% of the ice sheets, continuous layers mostly disappear and this part was widely characterized by the absence of any backscatter in older RES systems, had therefore often been referred to as echo-free zone (EFZ). While lacking RES system sensitivity failed to record weak backscatter (within the noise floor), earlier interpretations nevertheless also postulated that the EFZ was probably caused by deformed and stagnant ice, elevated englacial temperatures, or high layer roughness [5]. With improving radar imaging capabilities, subunits could be detected in this zone [6], now referred to as basal unit or basal layer instead of EFZ. Over the last decade, more and more locations have been identified where reflection anomalies appeared, up to hundreds of meters thick layers located between the conformly stratified internal horizons and the bed [7].

The existence of such ice subunits in the bottom part of the ice sheet, which differ from their overlying stratum by backscattering close to the noise floor and disturbed stratigraphy, indicates significant differences in the englacial dielectric properties. For most general purposes, we distinguish the radio characteristics in this basal unit between a low- and high-backscatter zone (LBZ and HBZ, respectively; see Section III-C in *Data and Methods* for details). Such backscatter changes in turn allow conclusions to be drawn about the physical properties at the base of the ice, as well as the processes that create them. Theories about the state

of the ice base and the processes that cause the peculiar reflections near the ice base are diverse. They range from frozen basal water on the underside of the ice sheet [6], [7], [8], [9], englacial folding [10], [11], [12], entrained subglacial material [13] to cold-temperate transitions with liquid water inclusions [14], [15], [16], [17]. Other explanations include sharp transitions in crystal fabric, heterogeneous small-scale roughness, stagnant ice, or disrupted isochrones [18].

Deciphering the material properties and physical conditions in the bottom part of the basal unit can, for example, improve our understanding of ice dynamics [18], hydrological processes [8], sediment transfer [19], the general availability of water and sediment in the subglacial environment [13], [20], and their effect on basal sliding [21]. Most notably, it is crucial to determine the different material compositions of the different subunits, which influence ice dynamics. In particular, for HBZs, the analysis based on the RES backscatter signatures seems appropriate to determine their physical characteristics and thus their significance for the ice-sheet system. For instance, if the lowermost HBZ is frozen to the bed, it could sustain the current ice configuration [22], accommodate only internal deformation without sliding, and thus keep ice-flow velocities low as well as protect the bed from erosional processes [8]. By contrast, if the lowermost HBZ indicates a temperate bed, destabilizing processes such as sliding with increased meltwater production, less sliding resistance permitting higher flow velocities, and increased erosion capacity may be more important.

The terms referring to the HBZ vary and are used inconsistently in the literature. Therefore, a variety of different descriptions of radar signatures fall under this term. Bell et al. [6] report "basal reflectors of several hundred meters in thickness, which are interpreted to be composed of a uniform distribution of point reflectors (diffuse reflectors) at the valley heads and valley walls of the Gamburtsev Mountains (East Antarctica)." They find two types of HBZ populations, one type with partly laminated reflectors and another type with a uniform reflection distribution. Winter et al. [13] detect a similar reflection signature in the near bed environment of the ice at the Independence Hills (West Antarctica), which they attribute to entrained sediment. These reflectors extend up to several hundred meters and are partly connected to the basal substrate. Another set of reflections in the near basal environment, which were attributed to entrained debris, were observed at the Hiawatha crater in the Greenland Ice Sheet [23]. A different type of reflection signature in the bottom part of the ice was found at Little Dome C [18] (East Antarctica), which is described as a notable change in return power between the continuous layering and the bed.

The question remains which dielectric properties and which associated material composition can be attributed to the respective backscatter patterns of the zones within basal units in the RES data. Electromagnetic (EM) simulators are a means to generate synthetic radargrams using a given medium with dielectric properties corresponding to those of typical near-bed environments of an ice sheet. For this, information about dielectric properties from ice cores and from materials found in the ice and at the base of the ice is required. A well-established method uses finite-difference time-domain (FDTD) models to investigate the nature of radar reflections in ice sheets in a 1-D domain [24], [25], [26], [27], [28]. Simulations in more complex geometrical environments in two and three dimensions can be conducted, for instance, with the open-source software gprMax [29], [30], which have been successfully used for glaciological applications [31], [32], [33].

II. Motivation

In this article, we present a conceptual study where we explore potential ice and material compositions that produce the radar signature of HBZs in basal ice units imaged with an airborne ultrawideband (UWB) radar system in the Jutulstraumen drainage basin in East Antarctica. For this purpose, we use the radar modeling software gprMax to compare synthetic radar signatures with the measured ones. We propose that the observed reflection signatures are most likely caused by point reflectors within the ice (e.g., originating from entrained sediments [13] or embedded basal material due to basal freeze-on [6]) of the basal units. Therefore, our focus is investigating the effects of point reflector concentration, size, and the dielectric properties of entrained material in the ice and at the ice–bed interface. In particular, the relationship between the return power and abruptness at the onset of the HBZ, the continuity of the return power within the HBZ, and the reflection properties at the ice–bed interface hold the potential to constrain or exclude possible material compositions.

III. Data and Methods

A. Radio-Echo Sounding Data

Here, we use RES data from an austral summer season 2018/19 airborne Antarctic radar campaign (JuRaS-2018; Jutulstraumen Radar Stratigraphy, Fig. 1) [34] conducted by the Alfred Wegener Institute, Helmholtz Centre for Polar and Marine Research (AWI). The data were acquired with AWI's multichannel UWB Multichannel Coherent Radar Depth Sounder 5 (MCoRDS 5) at an altitude of 365 m above ground. The radar system consists of an eight-element antenna array mounted underneath the fuselage of AWI's *Polar 6* BT-67 aircraft [35]. The radar data were recorded using three linear frequency modulated chirps at a 30-MHz bandwidth with a center frequency of 195 MHz (180–210 MHz). One measurement consists of three alternating waveforms to increase the dynamic range of the system (1-, 3-, and 10-μs chirps with increased receiver gain for the deeper-sounding waveforms). The near-bed environment is always covered by the high-gain 10-μs chirp. To reduce the data rate and to increase the signal-to-noise ratio (SNR), the recorded data from every channel were coherently presummed. For detailed data acquisition and instrument specification descriptions (see [36], [37], [38]).

We performed the data processing with the CReSIS Toolbox [40], which comprises pulse compression, synthetic aperture radar (SAR) processing (*f-k* migration), and array processing. To reduce sidelobes, we used a Tukey time-domain weighting on the pulse- and frequency-domain matched filtering with a Hanning window for pulse compression. For SAR processing, we used a two-layered EM wave propagation velocity model with constant dielectric permittivity values: $\varepsilon_{\text{ice}} = 3.15$ and $\varepsilon_{\text{air}} = 1$ for ice and air, respectively [41].

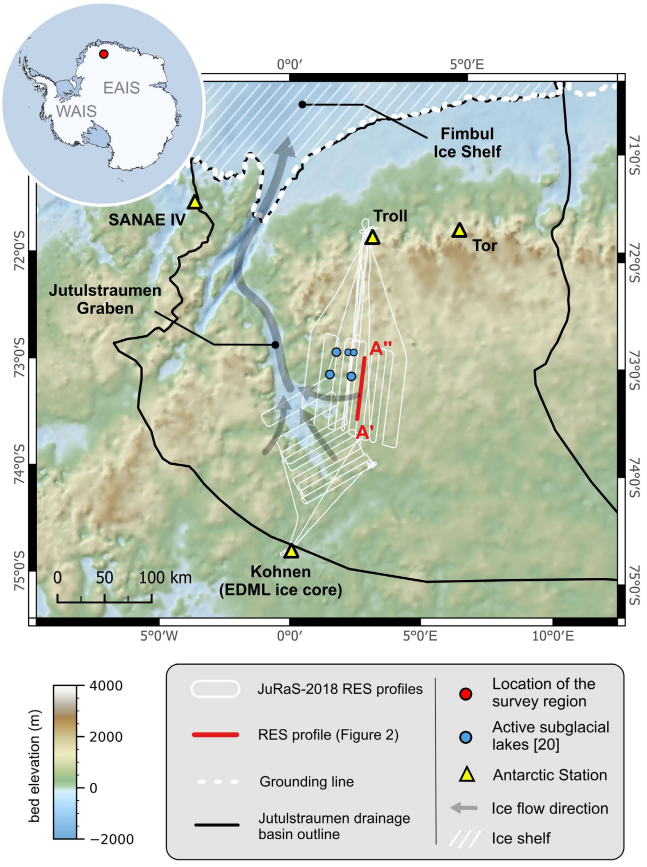

Fig. 1. Overview map showing the location of the Jutulstraumen drainage basin in East Antarctica, the location of the RES profile of Fig. 2 (red line), the location of the EDML ice core site, and the location of active subglacial lakes [20]. In the background, the BedMachine Antarctica bed elevation [39] is shown. The gray arrows schematically indicate the direction of ice flow.

One final radargram is composed of a total of 24 radargrams, whereby each consists pairwise of a combination of one of eight receivers and one of three waveforms [4]. Our final postprocessed radar data product has a horizontal along-track resolution of 15 m (trace spacing) and a range resolution of 4.3 m. For further details on radar data processing, we refer to Franke et al. [38], who processed similar data using the same methods and system parameters as the data used in this study.

For this study, we use two different radar data products (see Fig. 2). First, an unfocused SAR processed product [*qlook*; see Fig. 2(b)], which assumes that all reflections arrive at the receiver from nadir. Here, the data are coherently stacked along-track for each channel individually, and no correction for the propagation delay and no motion compensation are performed. Finally, all signals from each channel are averaged incoherently (cross-track). Second, a focused SAR (*f-k* migrated) data product [*standard*; see Fig. 2(c)]. For this product, coherent phase summation, as well as motion compensation with high-precision GPS and INS data, is applied. The antenna beam is steered toward nadir (delay and sum method) by coherent summation of each channel while considering each phase center measurement position. Furthermore, a Hanning window in the frequency domain is applied for sidelobe suppression. For the comparison with our gprMax simulations, we use the unfocused *qlook* data product since we do not perform any focusing with the gprMax results. However, we use the focused *standard* data to obtain information about true geometries of reflections near the base and from the ice–bed interface.

B. Survey Region and Glaciological Setting

The JuRaS-2018 radar data were acquired at the onset region of the Jutulstraumen ice stream [34], between the Troll (Norway) and Kohnen (Germany) stations (see Fig. 1). Most radar lines are oriented perpendicular to the direction of ice flow. They cover the deep central topographic depression (Jutulstraumen Trough), which prominently cuts through Dronning Maud Lands (DML) mountain chain where ice thicknesses range up to 3500 m. Furthermore, the radar lines cover the Jutulstraumen Ice Stream upstream region where smaller valleys merge into the Jutulstraumen Trough [34]. In addition, our northern survey lines cover a region of higher elevated topography and lower ice flow velocities in the East of the Jutulstraumen Trough. Franke et al. [34] classified this region as a preserved early-stage alpine landscape, where small-scale V- and U-shaped valleys indicate a low degree of glacial erosion. In general, the southern part of the Jutulstraumen drainage basin has most likely experienced a step-by-step development and subsequent modification of subaerial weathering and erosion by river systems and mountain glaciers until substantially preserved by a thick ice cover around 13.6 million years ago [34], [42]. Although this region is nowadays ice-dynamically stable, Neckel et al. [20] find evidence for an active subglacial hydrological system. They show that numerous topographic basins serve as reservoirs where subglacial water episodically collects and drains.

C. Radar Signature of the Bottom of the Ice Sheet

Fig. 2 shows a 65-km long RES profile located at the onset region of the Jutulstraumen Ice Stream east of the kilometer-deep Jutulstraumen Trough valley system (see Fig. 1). Ice thickness in this region ranges from 1.5 to 2 km and the subglacial topography is characterized by a mountainous landscape with elevation changes in several hundred meters. The top ∼75% of the ice column is composed of continuous internal layer stratigraphy, followed by a zone which includes nonlayered discontinuous patches of low backscatter and is partly echo-free [LBZ; see Fig. 2(a)]. Furthermore, we find continuous patches of high backscatter at several locations, which are located above the ice-base reflection [see Fig. 2(b)]. We term these units of high backscatter HBZs due to their prominent characteristic appearance in beneath the LBZ and proximity to the ice base.

The backscatter signature of the HBZs is characterized by consistently stronger return power with little variation compared to the LBZ. This suggests frequent changes in the dielectric properties between their onset and the ice base, similar to the layered radar stratigraphy in the upper part of the ice column. However, layering is not apparent in the radar signature of the HBZs. Moreover, the radar signature is nearly identical between the unfocussed (*qlook*) product and

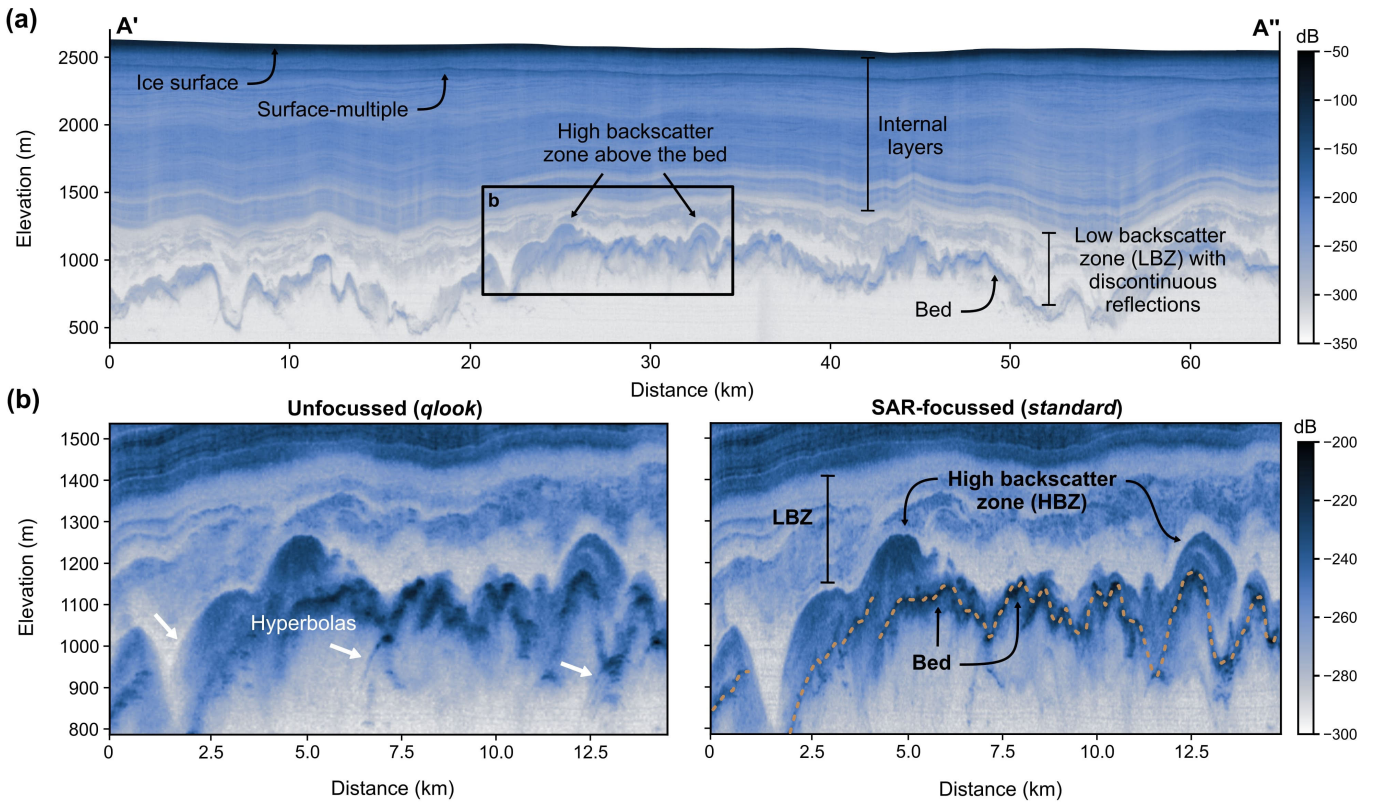

Fig. 2. (a) RES profile with the location indicated in Fig. 1. (b) Magnified views of the near-bed RES signature where patches of high backscatter (HBZ) are present above the bed reflection. The left radargram in (b) shows the unfocussed radar data product, whereas the right radargram shows the SAR-focused data product. Ice flow direction is into the page toward west-northwest.

the SAR-focused (*standard*) product [see Fig. 2(b) and (c)]. Unlike in the SAR-focused radargram, we find only a few indications of strong hyperbolic reflections in the unmigrated data [white arrows in Fig. 2(b)]. For a more detailed analysis of the backscatter pattern within the HBZs, we define three locations where HBZs (see Fig. 3) appear in the radargram and extract the A-scan of a single trace. For the selection of the individual A-scans as well as for further consideration in this study, we choose the (*qlook*) unmigrated data as they represent the closest analogy to the synthetic outputs created with gprMax.

The three HBZs considered here [HBZ1, HBZ2, and HBZ3; see Fig. 3(c)–(e)] are 100–200 m thick and located mostly on top of higher elevated topography in the radar profile [see Fig. 2(a)]. The radar signature throughout the HBZs is generally characterized by a relatively strong increase in backscatter at the boundary between the HBZs and the LBZ. In example, HBZ1 in Fig. 3, the backscatter decreases only marginally and remains high. For HBZ2 and HBZ3, there is more variation in backscatter within the HBZs but still remains at a high level (relative to the backscatter in the LBZ). Differences are also visible in the relation between the backscatter of the upper boundary of the HBZ and the backscatter at the ice–bed interface. In HBZ1, the bed reflection is almost nonexistent and most likely of similar strength as within the HBZ itself. In HBZ2, the bed reflection is of similar strength as at the onset of the HBZ, and in HBZ3, the bed reflection is stronger than the one at the HBZ onset.

Similar radar signatures of patches of higher backscatter above the bed reflection were reported in several studies in Antarctica and Greenland [6], [7], [13], [23], [43]. The nature of their reflections and the interpretation of the cause of the reflection signatures across the HBZs of these studies are diverse as well as their locations within the ice sheets and their ice-dynamic and overall glaciological context. We find the strongest similarities between our HBZ reflection signatures to the features found by Bell et al. [6], who describe the backscatter patterns for some of the hundreds of meter-thick basal reflectors along steep valley walls over the Gamburtsev Mountains as a "weak upper reflection underlain by a uniform distribution of point reflectors with no distinct laminations" [6] and hypothesize that the formation of the features is attributed to basal freeze-on processes. The existence of point reflectors in the ice, as well as the final proof of frozen subglacial water, is the best possible explanation at present, but could not yet be definitively validated. Also, Winter et al. [13] report patches of strong backscatter connected to the basal substrate and larger patches of point reflectors with hyperbolic returns above the bed, both of which they attribute to the entrainment of sediments. The sediment probably originates from the Horseshoe Valley (West Antarctica) and is entrained at the ice–bed interface by repetitive melting and freezing of warm-based ice. The fact that these characteristic backscatter features originate from point reflectors within the ice of HBZs were quantitatively analyzed using a Mie scattering model (i.e., scatterers' diameter on the order of the wavelength or larger) with

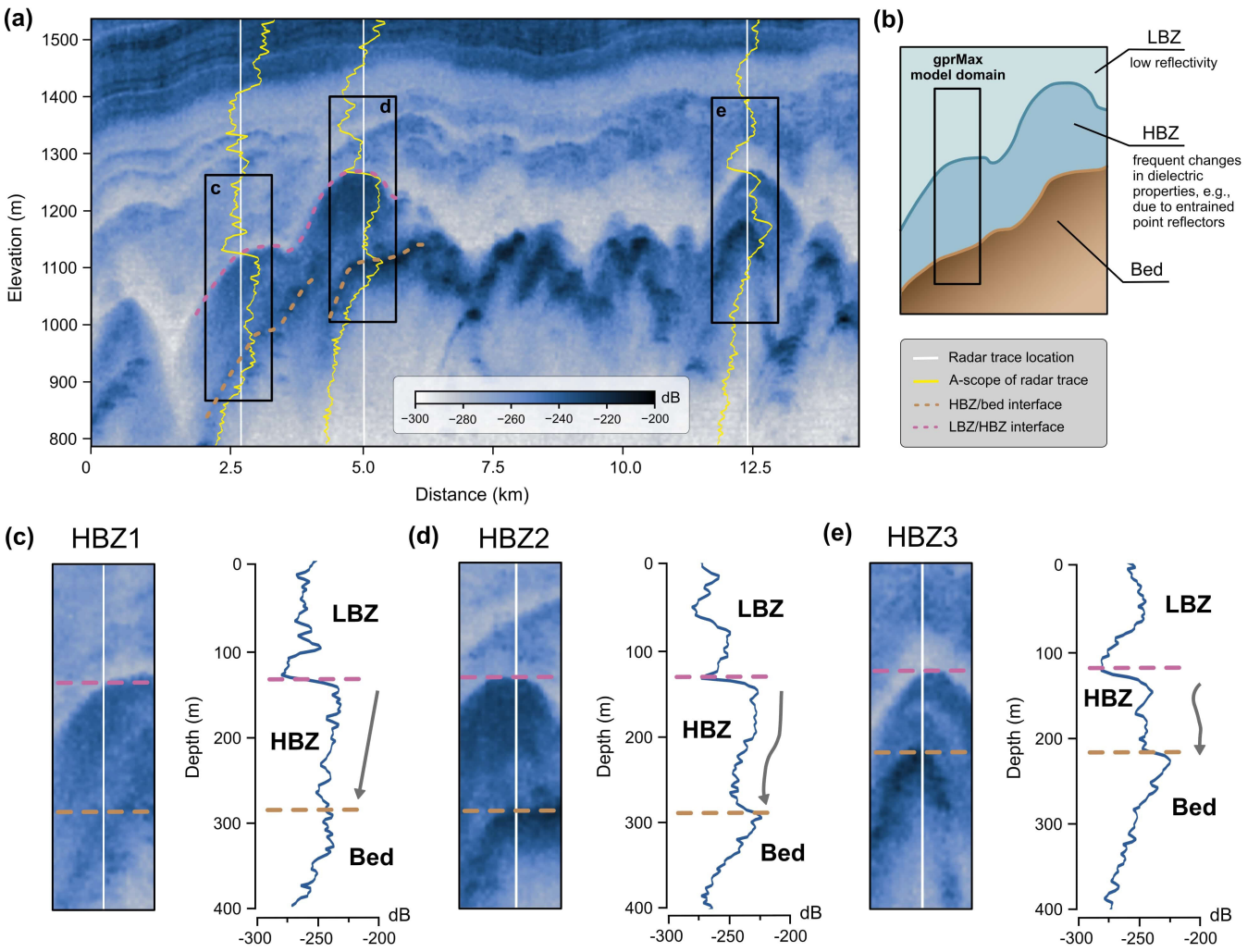

Fig. 3. (a) Same radar section as shown in Fig. 2(b) (unmigrated product, i.e., *qlook*). The locations of three HBZs (white vertical lines) are shown together with the respective A-scan at this location (yellow line). (b) Conceptual sketch of the near-bed backscatter properties and it includes the LBZ, HBZ, and the bed. (c)–(e) Three magnified views (radargram and A-scan) of three exemplary regions where thick HBZs are present.

a constant fractional volume of 10% [13], however not yet verified in-depth, especially with respect to the composition and particle concentration in the ice.

D. Electromagnetic Waveform Modeling With gprMax

The open-source software gprMax [29], [30] simulates the propagation of EM waves in 3-D space. The software solves Maxwell's equations using the FDTD method [44] and Yee cell [45], which has proved to be effective for 1-D simulations in deep ice [46], [47]. Continually increasing computing resources enable EM responses from larger and more realistic environments to be simulated. Models can be built using complex media, including several geometrical objects, layer roughness (topography) at material interfaces, dispersive and anisotropic materials, and heterogeneous mixing models. Moreover, gprMax includes a library of several predefined antenna models. gprMax supports parallelization of the FDTD solver using OpenMP for central processing units (CPUs) and using CUDA for graphics processing units (GPUs) [48]. We chose gprMax because it is open source and shows reasonable computation times for 2-D models with sufficient spatial resolution and, in particular, due to the improved treatment of model boundaries by perfectly matched layers (PMLs) [49]. Moreover, the material and model geometry input files are scriptable and, hence, a large number of complex models can be created with reasonable effort. All simulations shown here were produced with gprMax version 3.1.5 (Big Smoke).

E. Model Domain and Simulation Setup

For our simulations, we define a 2-D model domain (see Fig. 4) which extends 20 m in the x-direction (width) and 200 m in the z-direction (depth). By reducing the model depth (y-direction) to a single cell (0.02- or 0.01-m cell size), the electric and magnetic field components are set to zero in the invariant y-direction and the 3-D Maxwell's equations reduce to a 2-D form using the transverse magnetic mode. To avoid numerically induced dispersion [50], we keep the spatial discretization of our model more than ten times smaller than the smallest wavelength in the respective propagation media. In order to keep this criterion, the spatial discretization (cell size) in all three dimensions is 0.02 m for simulations

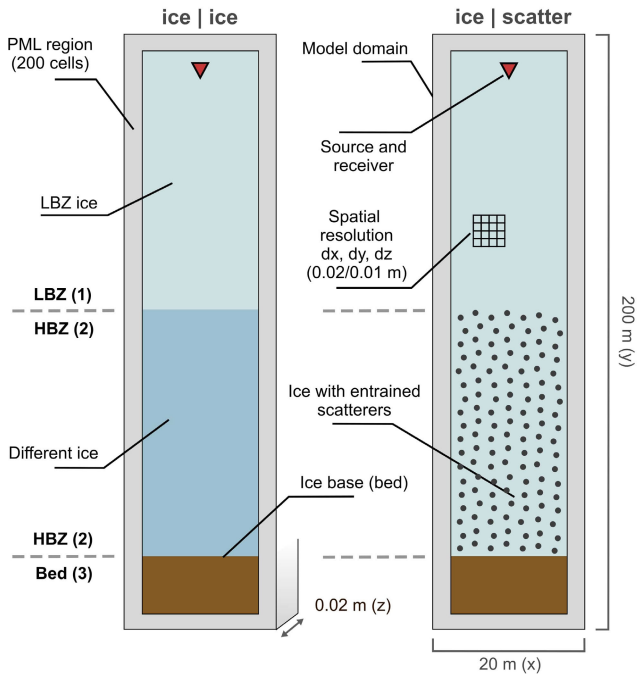

Fig. 4. gprMax model domain as indicated in Fig. 3(b). The material through which the simulated radar wave propagates is composed of three parts: 1) an LBZ composed of pure ice; 2) an HBZ, which is composed of pure ice with slightly different dielectric properties as the LBZ ice on the left sketch (ice | ice) and composed of LBZ ice but with entrained point reflectors on the right sketch (ice | scatter); and 3) the ice–bed interface. The entire model domain is surrounded by a PML absorbing boundary condition of 200 cells.

using solid input materials and 0.01 m for simulations with high-permittivity materials, such as subglacial water. The time step Δt is 0.0472 ns for 0.02-m cell size simulations and 0.0236 ns for 0.01-m cell size simulations, which satisfies the Courant stability criterion [44].

The transmitting antenna (tx) and receiving antenna (rx) are placed 10 m below the upper limit of the model domain and in the center along the x-axis (see Fig. 4). To ensure that the signal penetrates the entire model depth under different permittivity scenarios, we run the simulations for a time window of 2.5 μs. The antenna type represents a Hertzian dipole transmitting a Ricker wavelet polarized in the y-direction. For all our simulations, we use a fixed frequency of 195 MHz, which corresponds to the center frequency of the JuRaS-2018 RES survey. At the outer boundary in the x- and z-direction, we define 200 PMLs (see [29]) cells (4.0 m) as our absorbing boundary condition. The required amount of PML cells was determined in a prestudy with the objective of muting all reflections at the model domain boundaries from transmitted or reflected radar waves. All associated model parameterizations are summarized in Table I. Our gprMax simulations ran on an HPC on CPU nodes (2.3 GHz) with 36 cores and 62-GB RAM. Simulations required approximately three hours with 0.02-m resolution and approximately 17 h with 0.01-m resolution.

The model domain represents a subregion of the total ice sheet that focuses on the near-bed environment of the ice sheet, where the HBZs are mapped [see Fig. 3(b)]. The radar wave propagating through the upper part of the ice column is therefore ignored. This is justified by the fact that computation time is significantly reduced as well as by the assumption that, for the purposes of our study, changes in the wavefront due to the propagation through the upper ice column do not have a significant effect on the analysis of relative return power values. There are three categories of materials in the model domain. We attribute the dielectric properties of the upper 100 m of the entire model domain to ice, which has been measured by dielectric profiling (DEP) [5], [51], at the EMDL ice core. Below, we define an 80-m-thick region representing the HBZ. This thickness represents the average thickness of HBZs found in the survey region. The HBZ is either composed of homogeneous ice, similar to the LBZ or composed of point reflectors. The particle size of the point reflectors cannot be smaller than the cell size of the model domain. Hence, with this setup, we are able to represent point reflectors with a minimum diameter of approximately 2 cm. The third layer (20 m thick) represents the bed below the HBZ at the bottom of the model domain.

TABLE I
GPRMAX KEY MODEL PARAMETERS

Variable	Value	Comment
Domain (x,y,z)	20, 0.02/0.01, 200 m	2D domain
dx, dy, dz	0.02, 0.02, 0.02 m 0.01, 0.01, 0.01 m	0.01 m for simulations with liquid water
Time window	2.5 µs	
Time step	0.0472 ns 0.0236 ns	0.02 m resolution 0.01 m resolution
Iterations	52 998 105 994	0.02 m resolution 0.01 m resolution
Waveform type	Ricker wavelet	
Frequency	195 MHz	JuRaS-2018 survey centre frequency
Antenna type	hertzian dipole	polarized in y
tx position (x,y,z)	10, 0, 190 m	zero offset
rx position (x,y,z)	10, 0, 190 m	zero offset

We performed simulations in two types of HBZ material compositions (see Fig. 4). In the first one, we assume that the HBZ represents a single transition from the LBZ ice to homogeneous ice with slightly different conductivity. This would resemble, for example, a freeze-on layer of pure subglacial water. For the second type of simulations, which represent the bulk of model runs, we assume that the HBZ is composed of point reflectors, which are embedded in the LBZ. To avoid layering, the point reflectors are not arranged at regular spacing but with small random offsets in the x- and z-directions. For the representation of point reflectors in the HBZ region, we use the gprMax cylinder objects.

F. Simulations

We performed simulations for different material composition scenarios to target the following questions.

1) How does the radar signature between an HBZ composed of pure ice differ from the signature of an HBZ composed of any sort of embedded point reflectors?

TABLE II
MATERIAL PARAMETERS—FOR INPUT PARAMETERS IN GPRMAX, WE SET ALL OUR MATERIALS TO BE NONMAGNETIC AND THEREFORE THE RELATIVE PERMEABILITY $\mu_r = 1$ AND THE MAGNETIC LOSS $\sigma_* = 0$

material	relative permittivity (ε_r)	conductivity (σ)	reference	comment
LBZ ice	3.15	0.01 mS/m	permittivity: [52] conductivity: [5], [51]	σ: 0.01 – 0.03 mS/m [5], [51]
HBZ ice	3.15	0.03 mS/m	permittivity: [52] conductivity: [5], [51]	
Low-dielectric rock	4.0	0.1 mS/m	permittivity and conductivity: [53], [54]	derived from average values for frozen bedrock, dry sand and granite[a]
High-dielectric rock	8.0	1.5 mS/m	permittivity and conductivity: [53]–[55]	derived from average values for limestone and shale[b]
Subglacial water	88.0	40.0 mS/m	permittivity: adopted from [55] conductivity: adopted from [56]	

[a] Frozen bedrock [53]: ε_r = 2.7, σ = 0.01 – 1.0 mS/m; dry sand [54]: ε_r = 3 – 5, σ = 0.1 mS/m; granite [54]: ε_r = 4 – 6, σ = 0.01 – 1.0 mS/m
[b] Limestone [54]: ε_r = 4 – 8, σ = 0.5 – 2.0 mS/m; shale [54]: ε_r = 5 – 15, σ = 1.0 – 100.0 mS/m

2) What is the effect of particle size and volume fraction of the embedded point reflectors on the radar signature?
3) How do different dielectric properties of the point reflectors affect the reflection in combination with varying dielectric properties of the bed?

The simulations are divided into four categories.

1) Single Material Transition: For this scenario, we assume that the HBZ represents ice with slightly different conductivity than the ice in the LBZ [setup shown in Fig. 4 (left)].

2) Point Reflectors With Variable Particle Size: Here, we assume that the HBZ is composed of a large number of point reflectors embedded in the LBZ. The dielectric properties of the matrix ice are those of the LBZ. Each point reflector represents a change in dielectric properties and the zone composed of these point reflectors represents the HBZ [setup as in Fig. 4 (right)]. Point reflectors are placed between 20 and 100 m (note that the bottom-left corner of the model domain represents the origin of the coordinates) into the LBZ with a total volume fraction of 10%. In this scenario, we test the signature of the reflected radar wave for the effect of changes in particle sizes for particles with 2-, 4-, 10-, 20-, 40-, and 100-cm diameter. The choice of the range of sizes of the point reflectors is given by the smallest possible particle size in our model (2 cm) and plausible particle sizes found in the field (West Antarctica) [13].

3) Point Reflectors With Variable Volume Fraction: Here, we keep the particle size constant at 4-cm diameter [13] and investigate the variation of the total fraction of point reflector volume in the total volume between 1% and less than 100%. The total volume fraction is distributed homogeneously in the area defined as HBZ. We justify our chosen volume fraction range by measured englacial debris concentrations in Antarctica of approximately 0.3%–20% [13], [19], [57], [58]. Also, higher debris concentrations up to 50% are theoretically possible, as shown in a modeling study [59]. With regard to possible concentrations of liquid water content (LWC), the concentrations which have been determined in temperate and polythermal glaciers range between ~0.1% and 10% [60], [61]. Although realistic values of LWC for glaciers are on average in the lower percentage range, we also test higher concentrations compared to other particle materials.

4) Point Reflectors With Variable Dielectric Properties: All simulations with different volume concentrations of point reflectors are carried out for three different dielectric properties: 1) low-dielectric rock material; 2) high-dielectric rock material; and 3) subglacial water (see Table II). This allows us to study the effect of changing point reflector concentration as a function of typical dielectric materials of entrained particles in ice. In addition to the point reflectors, we also run simulations in all possible constellations for different dielectric properties at the glacier base.

G. Input Materials

Input materials in gprMax require four constitutive parameters: 1) the relative dielectric permittivity ε_r; 2) the electric conductivity σ; 3) the relative magnetic permeability μ_r; and 4) the magnetic loss factor σ_*. The materials in our simulations are considered nonmagnetic, thus for all materials, we set the relative magnetic permeability $\mu_r = 1$ and the magnetic loss factor $\sigma_* = 0$. For modeling the radar response of the HBZs, we use the following materials, whose exact dielectric properties are listed in Table II.

1) LBZ Ice: Ice representing the almost EFZ with homogenous material composition. The dielectric properties were derived from DEP conductivity measurements [62] in the EFZ of the EDML ice core [5], [51]. We define the lower bound of [5] and [51] for the conductivity with $\sigma = 10$ μS/m. The relative permittivity is set to $\varepsilon_r = 3.15$.

2) HBZ Ice: Pure ice with a similar composition as in the LBZ but with slightly higher conductivity represents slightly different ice from the LBZ. This material represents the scenario when the HBZ is composed of accreted basal ice due to basal freeze-on without entrained point reflectors. As we are not aware of any direct dielectric measurements on refrozen subglacial water, the conductivity is defined as the upper bound of [5] and [51] with $\sigma = 30$ μS/m and the relative permittivity is set to $\varepsilon_r = 3.15$.

3) Low-Dielectric Rock: For the implementation of low dielectric point scatterers and a low-dielectric ice base,

we define a low-dielectric rock material. The values for conductivity and relative permittivity represent average dielectric properties from measurements of frozen bedrock [53], dry sand [54], and granite [54] ($\sigma = 100$ μS/m and $\varepsilon_r = 4.0$).

4) High-Dielectric Rock: A high-dielectric rock material is defined as the second type of point reflectors and ice base material with average values for relative permittivity and conductivity of high-dielectric rocks, such as limestone [54] and shale [54]. The relative permittivity was set to $\varepsilon_r = 8.0$. The conductivity value was set to $\sigma = 1.5$ mS/m to be within the range of limestone and shale and to represent a value that lies between the low-dielectric rock material and subglacial water.

5) Subglacial Water: For the scenario that the point reflectors or the material at the ice base are at the pressure melting point and liquid water (in this case, a subglacial lake) is present, we define a subglacial water material based on the dielectric properties by Tulaczyk and Foley [55] (for relative permittivity; $\varepsilon_r = 88.0$) and Christner et al. [56] (for conductivity; $\sigma = 400$ mS/m). The subglacial water is implemented as liquid water inclusions in the same way as the point scatterers.

H. Signal Processing

The following processing steps were applied to compare field RES observations of the JuRaS-2018 campaign and the synthetic radar data generated with gprMax. We derived the reflected energy P of the synthetic radar data following [47] by calculating the envelope of the electric field strength (E_y component) applying a Hilbert magnitude transform. In addition, the trace was smoothed with a 1-D Gaussian filter with a standard deviation of 5 to filter a considerable amount of high-frequency signal content, which is introduced from the simulation (e.g., from the raw source Ricker wavelet). This enables us to better mimic the impulse response of the real transmitted signal and reflections at an interface (e.g., that a reflection from a flat interface will be displayed as a single strong reflection). Finally, we obtain the signal power by converting the electric field envelope into dB [$20\log_{10}(E_y)$]. We applied no corrections for englacial attenuation or geometrical spreading of the radar wavefront neither for the observed (unmigrated) RES data nor for the synthetic RES data. In contrast to the synthetic single trace data, a single trace of the field data (*qlook* product) contains coherent array processing due to the eight-element antenna array and incoherent along-track stacking. However, this difference should not affect the general appearance of the reflected power in the HBZs.

Based on the signal processing and considering the radar wavelength of our simulations with a frequency of 195 MHz in ice, we can determine the range resolution (the ability to distinguish two reflectors). For this, we take the full width at half maximum of the simulated reflection for the ice-ice interface (e.g., the red lines in Figs. 5 and 6), which is ~25 ns in two-way traveltime, corresponding to 2.1 m of range resolution for our simulations.

IV. Results

As illustrated in Fig. 5, there is a fundamental difference between the simulated radar reflections of the HBZ, which is composed of homogeneous ice and the one composed of embedded point reflectors [note that the radargram-like plots in Fig. 5 (right) are 1-D and represent respective single traces reproduced multiple times to mimic a radargram]. In the ice-to-ice transition case, there is a reflection at the transition between LBZ and HBZ with an immediate decrease in return power within the HBZ and another reflection at the ice–bed interface (red lines in A-scans in Fig. 5). For HBZs that consist of point reflectors, in addition to the strong reflection at the transition between the LBZ and the HBZ, there is also a significant variation in return power within the HBZ depending on particle concentration and dielectric properties [see Fig. 5(b) and (c)]. Yet the backscatter within the HBZ is generally high. In Sections IV-A–IV-C, we present the results of a systematic analysis of the effects of point reflector size, concentration, and dielectric properties, respectively.

A. Variations in Point Reflector Size

We consider circular particle sizes with a diameter of 2, 4, 10, 20, 40, and 100 cm at a constant particle concentration of 10% in the HBZ [see Fig. 5(a)]. Consequently, for simulations with small point reflectors, a higher amount of reflectors are embedded in the ice than for simulations with large reflectors to maintain the same particle concentration. To avoid regular stratification, the point reflectors are distributed nonuniformly over the entire HBZ area with small offsets in the x- and z-directions. Fig. 5(a) shows the individual A-scans for all particle sizes, as well as the simulation without point scatterers for comparison. In the plots on the right, the same simulations are shown individually as radargrams. All simulations were conducted with the low-dielectric rock material parameters for the point scatterers in the HBZ and the bed.

The simulations with entrained point reflectors show an increase in backscatter at the onset of the HBZ, followed by a relatively constant return power with a slight linear decline within the HBZ. The reflection at the ice–bed interface stands out from the lower part of the HBZ, but it is weaker than the reflection at the onset. No significant differences in the backscattering behavior between the different particle sizes are apparent. Within the HBZ, there is a similar decay and a similar magnitude of return power at the onset and end of the HBZ. Similar simulations have also been conducted using the high-dielectric rock material properties for the point reflectors in the HBZ and at the bed, showing equally similar results (not shown here). Even though they show a different signature with a stronger decrease in return power within the HBZ, the results between the different grain sizes are nearly identical at constant concentrations in the ice. Therefore, we can assume that at constant particle concentration in the ice, a change in grain size (within the range of particle diameters tested here) does not significantly alter the reflection signature within the HBZ.

B. Variations in Point Reflector Concentration

For most of our simulations, we changed the concentration of particles embedded in the ice. The particle size is kept

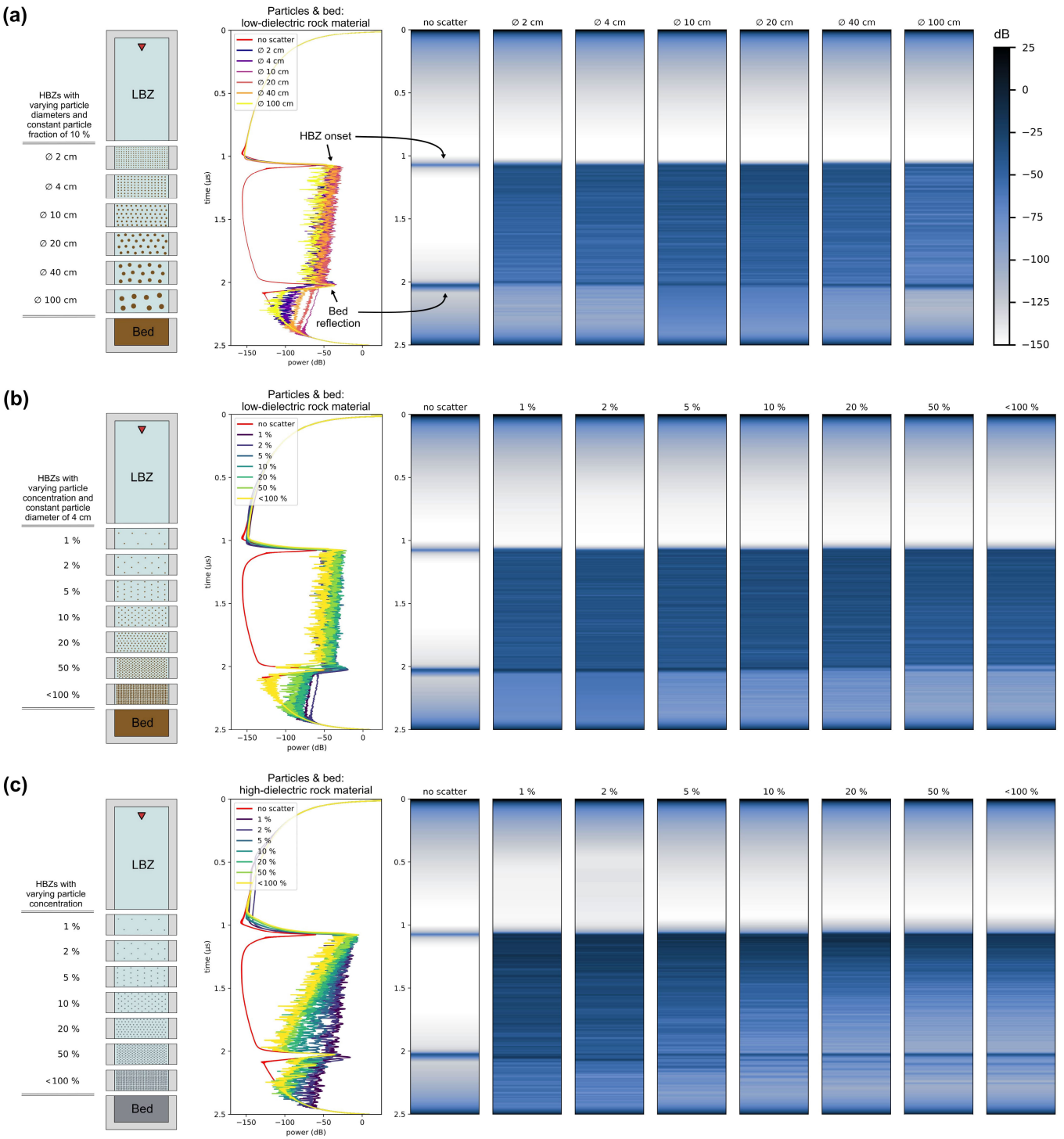

Fig. 5. gprMax simulation results with different HBZ (a) particle sizes and (b) and (c) particle concentrations. The left column shows a sketch with the key properties of the simulations. The A-scans of all respective simulations (color coded) are shown to the right as well as all individual simulations as radargrams. Note that the radargram-like representation of the A-scans represent a single trace (1-D) reproduced multiple times to mimic a radargram. The black arrows in (a) link the HBZ onset and bed reflection between the two forms of representation of the simulated radar trace.

constant at 4-cm diameter, which corresponds to the average size of measured rock sizes in ice [13]. Our simulations are performed for particle concentrations of 1%, 2%, 5%, 10%, 20%, 50%, and <100% in the ice. The case for <100% represents an extreme case that is unlikely to occur in natural basal ice. However, we still consider this case to fully cover the investigation of trends of increasing particle concentration. As the sum of circular cross sections of the point reflectors in gprMax is equal to the area of the HBZ, the specification of <100% refers to the fact that some particles overlap in area due to the random offset in x and z-directions, thus resulting in a less than 100% area for the point reflectors in the HBZ.

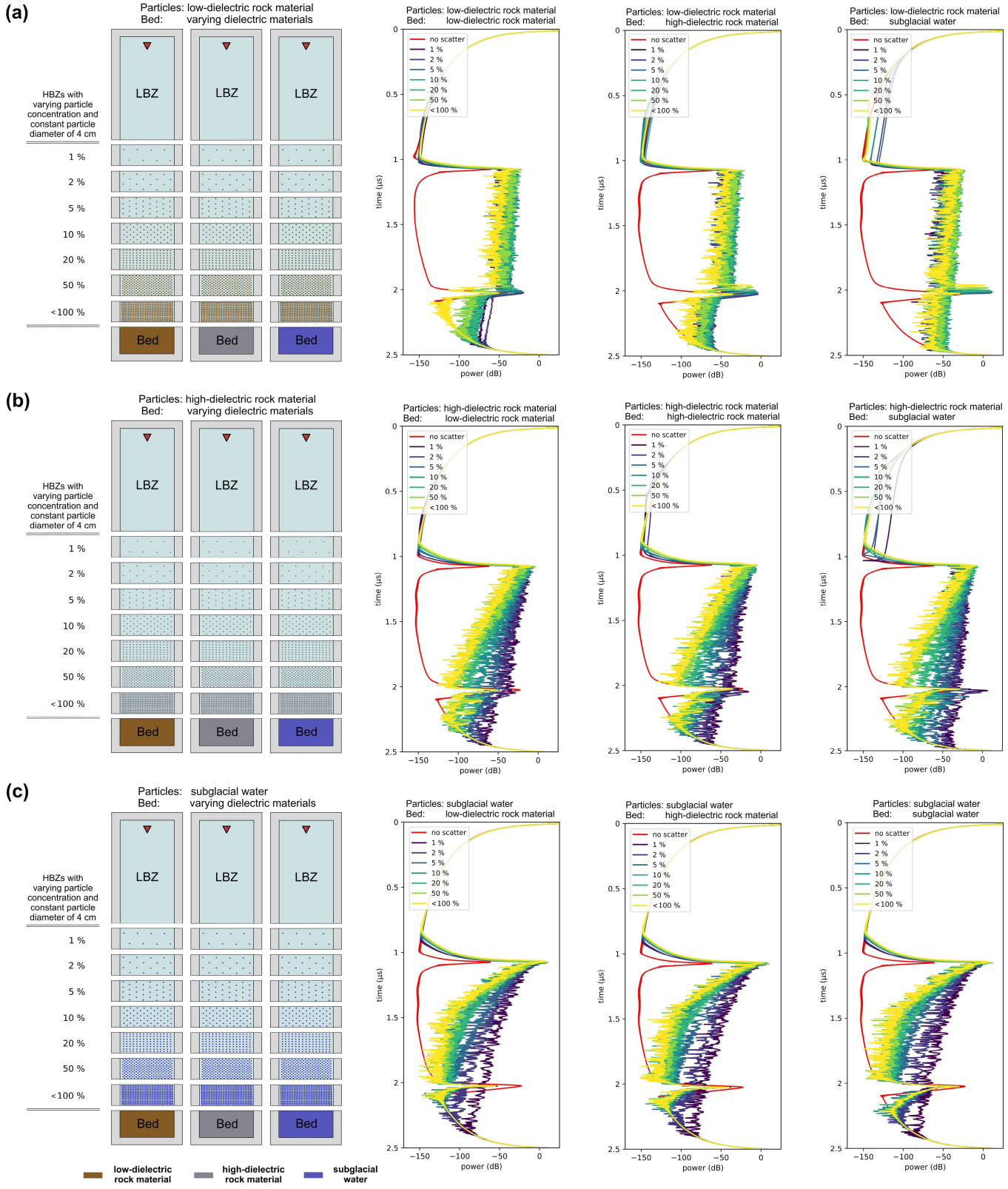

Fig. 6. gprMax simulation results of different particle concentrations in the HBZs for different dielectric material scenarios for the entrained particles as well as for the bed. (a) Results for simulations where the entrained particles are composed of low-dielectric rock materials. (b) Results for high-dielectric rock material particles. (c) Results for particles composed of liquid water in the HBZs. The results are shown as A-scans for three different material properties of the bed. The key simulation parameters are schematically shown in the left column.

In Fig. 5(b) and (c), the radar responses for particle concentrations from 1% to <100% are shown for low-dielectric rock material and high-dielectric rock material. The respective material properties apply to both the point reflectors and the bed. In addition, the radar response of the ice-to-ice transition scenario is shown for reference. We observe a reflection behavior similar to that shown in Fig. 5(a) in the simulations using the low-dielectric rock material. There is an increase in backscatter at the transition to the HBZ, and the return power remains constant within the HBZ with a slight linear decrease until the bed reflection [see Fig. 5(b)]. The only exception is the case with <100% particle concentration, where the linear decrease in return power is slightly stronger.

For the high-dielectric rock material, the signature of the backscatter in the HBZ with increasing particle concentration [see Fig. 5(c)] is clearly different from that for the low-dielectric rock material [see Fig. 5(b)]. The reflection at the onset of the HBZ is significantly stronger (∼20 dB) than in the low-dielectric case, but the backscatter within the HBZ already decreases significantly with depth at low particle concentrations. This decrease of the return power, i.e., the mean power gradient, in the HBZ becomes stronger with increasing particle concentration (approximately between −15 and −100 dB within the HBZ). At the transition to the bed, a strong reflection can be observed in all cases, which, however, is smaller in magnitude (∼30 dB smaller) than between LBZ and HBZ.

C. Variations in Dielectric Properties

The reflection properties at the base of the HBZ, within the HBZ, and at the transition to the ice base are strongly affected by the concentration of point reflectors in the ice as well as their dielectric properties (as well as those of the bed). Therefore, we ran simulations with all possible combinations of dielectric materials (low- and high-dielectric rock and subglacial water) with their respective particle concentrations ranging from 1% to <100%. Fig. 6 shows the results for all nine combinations. The top row shows the results for the low-dielectric rock material in the HBZ as point reflectors but with different bed materials. The middle row represents the high-dielectric rock material in the HBZ and the bottom row is an HBZ containing liquid water droplets with different bed materials, respectively. Generally, the higher permittivities and conductivities of the high-dielectric rock material and subglacial water result in stronger bed return power. In the case of point scatterers consisting of low-dielectric rock material, the return power of high-dielectric rock material and subglacial water is stronger than that at the base of the HBZ.

There is also a stronger bed reflection for higher dielectric properties for HBZs that are entrained with high-dielectric rock materials. However, the ice-base reflection is only stronger as the HBZ onset reflection for the case where the base is composed of liquid water. The greatest loss of return power occurs when the HBZs are composed of liquid water inclusions (approximately –70 dB for 1% LWC to −120 dB for <100% LWC between the top of the HBZ and the base of the HBZ). Furthermore, here, the bed reflection amplitudes are the smallest of all scenarios. If the HBZ contains an LWC of 1% and the bed consists of low-dielectric rock material, the basal reflection is so low that it cannot be distinguished from the reflections within the HBZ. At this low concentration of liquid water inclusions, the basal reflection is not visible except if the bed is composed of high-dielectric rock material or liquid water inclusions.

We note that the effect of particle concentration (or LWC) is stronger if the dielectric properties of the entrained particles are higher. Also, if the dielectric properties of the point reflectors are high and particle concentration is low, it is more difficult to determine the ice-base reflection. The bed reflection becomes more apparent at these low concentrations if the dielectric properties of the bed are sufficiently high, thus increasing the dielectric contrast between the HBZ and the bed and yielding a larger reflection coefficient.

D. Comparison Between Measured and Modeled Data

We restrict the comparison of the modeled radar signatures of the HBZs in gprMax in Fig. 6 and the measured ones in Fig. 3 to the relative shape of the backscatter pattern in dB at the onset of and inside the HBZ as well as at the bed reflection. For the measured radar signatures, we have three different cases: (HBZ1) slightly decreasing return power (small gradient) inside the HBZ and weak reflection at the bed [see Fig. 3(c)], (HBZ2) a gradual decrease of return power inside the HBZ and similarly strong reflection at the HBZ onset and at the bed [see Fig. 3(d)], and (HBZ3) almost constant return power inside the HBZ (i.e., zero gradient) with slight variations and stronger reflection at the bed than at the top of the HBZ [see Fig. 3(e)]. The results of the radar simulations with the greatest similarities to the radar signatures of the HBZs are summarized in Fig. 7.

The shape of the backscatter in HBZ1 bears the strongest similarities to the simulations with the low-dielectric rock material [see Fig. 7(a)]. The return power within the HBZ is nearly identical for all particle concentrations simulated here between 1% and <100%. The decrease in return power is too high for the cases with the higher dielectric material properties HBZ2 and HBZ3 [see Fig. 6(b) and (c)]. However, it is conceivable that the same radar signature can be achieved with higher dielectric material properties than in HBZ1 but with a very low particle concentration [e.g., 1% high-dielectric scatter; see Fig. 7(a)]. The slight decrease in return power in the lower part of the HBZ in case HBZ2, as well as the equally strong reflection strength at the bed and at the base of the HBZ, could indicate a low-dielectric rock material in low concentration in the upper part of the HBZ. Within the HBZ, however, an increase in particle concentration might result in a larger return power loss. The slightly stronger bed reflection could be caused by a basal material with higher dielectric properties than what is embedded in the HBZ [see Fig. 7(b)].

The radar signature in HBZ3 is similar to that in HBZ2, except that there is slightly more variation in return power within the HBZ. We have not specifically tested such a case in our simulations. However, we can assume that the almost constant average strength of the return power within the HBZ is also related to an embedded low-dielectric rock material.

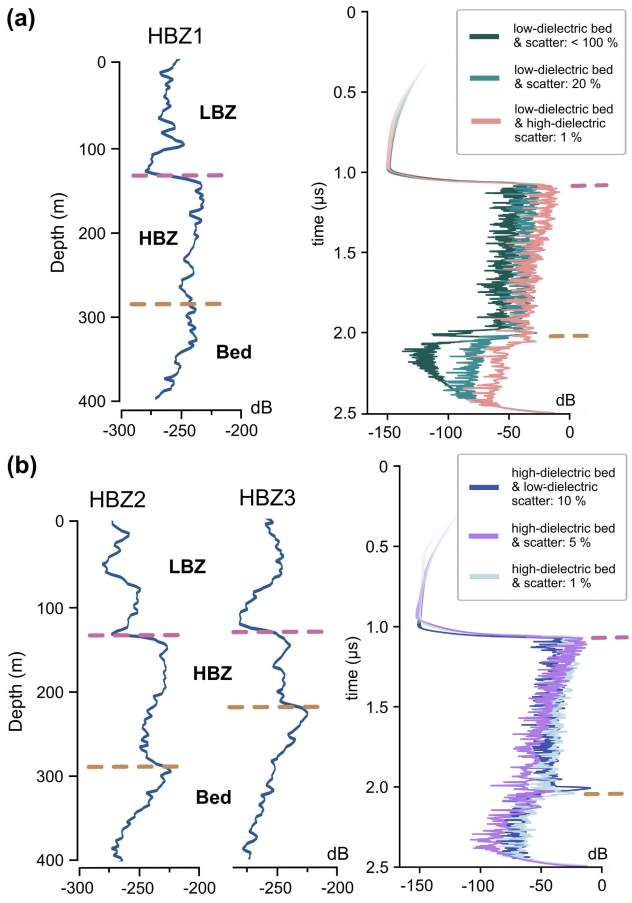

Fig. 7. Comparison between (left) measured and (right) best-fit simulated A-scans. Comparison for the radar response in (a) HBZ1 and (b) HBZ2 and HBZ3 (see Fig. 3).

Possibly, layers within the HBZ with an absence of embedded particles could create such a drop in return power as observed in HBZ3. The difference in backscatter at the bed is even stronger than in HBZ2, possibly corresponding to an even higher dielectric contrast between the material inside the HBZ and at the bed [blue trace in Fig. 7(b) (right) representing an HBZ with 10% low-dielectric scatter and a high-dielectric bed]. Furthermore, HBZ1, HBZ2, and HBZ3 show the greatest discrepancy to all simulations in which the HBZs contain liquid water [see Fig. 6(c)]. We would also like to emphasize that these comparisons between measured and simulated radar data are carried out under the best possible setting for the simulations, which nevertheless contains limitations that are listed in the discussion and therefore cannot be transferred one-to-one.

V. Discussion

The modeling presented here is not intended to determine the exact material properties due to several limitations outlined below. Our motivation is instead to constrain particular scenarios as likely or unlikely, for example, whether an HBZ consists of pure ice, ice with entrained sediment, or temperate ice with liquid water inclusions. It represents a reasonable approximation that allows us to discriminate between extreme cases on the spectrum of dielectric properties for materials that are likely present in the ice close to the bed. For a more precise determination, the full consideration of the entire modeling domain and further complementary geophysical measurements such as seismic methods or high-resolution radar measurements using phase-sensitive radio-echo sounders are recommended. Moreover, in addition, information about the basal thermal state and subglacial hydrology from modeling [8], [22], [63], [64], as well as geological information from nearby outcrops or blue ice areas with entrained clasts [13], provide additional information to constrain the HBZ properties, such as particle size, the dielectric properties and concentration of entrained particles. Ultimately, as in many cases, the exact and small-scale composition of the material that makes up the HBZ in the radar data can only be determined with in situ measurements of drilled ice cores.

Based on the results presented here, we hypothesize that the backscatter signature in the unit we classify as HBZ originates from embedded point reflectors in the ice. We justify this primarily by noting that the measured return power within the HBZ is nearly uniformly high in many cases, suggesting a steady change in dielectric properties. This is consistent with the conclusion that embedded point reflectors determine the backscatter pattern, which has been raised in several previous studies (see [6], [13]) where similar basal reflection signatures were found. We exclude reflections caused by changes in the crystal orientation fabric [51] from possible explanations for the observed HBZ reflections, as these are unlikely to appear for 100–200-m-thick units and at such backscatter strengths.

The reflection anomaly which we term HBZ is not specifically defined in the glaciological community. The units that we define as HBZ in the Jutulstraumen drainage basin are, therefore, one particular example out of many (e.g., those found by Bell et al. [6], Winter et al. [13], Lilien et al. [18], or Kjær et al. [23]). As diverse as the radar signatures and, thus the possible compositions and physical properties of the HBZs are, so are the hypotheses for their formation. With the assumption that the HBZs in the Jutulstraumen drainage basin may consist of ice entrained with englacial debris, considerations can subsequently be made about the embedding processes (e.g., through basal freeze-on in combination with regelation [6], [59], [65] or other processes of entrainment [13]). With respect to the occurrence of our HBZs in an alpine subglacial setting on high-elevated subglacial topography [34], we see the strongest similarity to the HBZs investigated in the East Antarctic Gamburtsev Mountains [6]. The thickness of HBZs with this reflection pattern also allows conclusions to be drawn about the underlying processes in and history of the ice sheet. Assuming that local or widespread processes like regelation (sliding-induced melting-refreezing), general ice accretion (i.e., basal freeze-on which assumes that additional ice is added at the base of the ice column), or other embedding processes produce the HBZ of entrained sediment packages [66] might provide information on past hydrological conditions, the thermal state of the ice base, and the mechanism of sediment transfer [19]. However, decoding this information is beyond the scope of this study and requires additional investigations.

A. Insights From the Comparison Between Field Observations and Synthetic RES Data

Here, we focused on simulating extreme cases of particle concentrations and extreme cases of dielectric variations in the ice. Some of the scenarios we have modeled are unlikely to represent the real composition within an ice sheet. However, they provide useful insights into the interpretation of radar signals from basal units. In particular, we can clearly see the effects of trends in particle concentration in combination with end members of possible dielectric properties of entrained point reflectors. Particles embedded in ice produce a range of backscatter signatures and energy decay within the HBZ. The backscatter at the top of the HBZ is thus dictated by the bulk dielectric properties of the entrained particles. Based on our simulations, backscatter, as in the Jutulstraumen HBZs, is most likely caused by embedded particles with low dielectric properties. The particle size of the scatterers does not seem to play a significant role in the backscattering within the limits we tested (at a wavelength of 86 cm in ice), as long as the total particle concentration remains constant. As our particle sizes range between 4 and 100 cm in diameter, we are largely within the range of Mie scattering. This could be an explanation for the fact that the backscatter in the HBZ does not change significantly with changing particle size but constant particle concentration.

B. Limitations and Uncertainties

Our model setup represents a simplification of the complex environment near the base of the ice sheet. Therefore, any interpretation attempting to infer one-to-one the material composition of the HBZs and the dielectric properties of the ice base should be considered with caution. In our 2-D experiment, it is not possible to represent the entire wavefield and, thus, the true amplitudes within our model domain. Moreover, due to computational limitations, we cannot simulate very small particle sizes since the particle diameter cannot be smaller than the cell size. Small objects, like millimeter-scale sediment grains or water droplets or veins, would require ten to hundred times higher resolution of the model domain, resulting in very long computation times. However, as our particle sizes are already covering the size range from the wavelength of the source signal (86 cm) down to almost two orders of magnitude less, we do not expect major differences by further decreasing the size of the scatterers. For scatterers larger than the wavelength of our signal, we would expect a less continuous influence on backscatter properties. If they were spaced beyond the size of the first Fresnel zone, a more discrete pattern of high backscatter could be expected, as was, for instance, observed in the Hiawatha Glacier in Greenland (see [23, Fig. 5(E) and (G)]).

In our model environment, we ignore the upper ∼80% of the ice column as well as the distance between ice surface and radar antenna and place our transmitters and receivers 100 m above the HBZs. Thus, the englacial attenuation and further influence on the wavefield and wavefront in the field data are not reflected in our simulations. The size of the pulse-limited footprint is also smaller in our simulations compared to the survey RES data due to the relative distance of the instrument. The footprint size has an influence on the illuminated volume (and thus the number of illuminated particles) of the scattering medium and therefore an influence on the returned power. This effect is unfortunately not shown here due to the limited geometry size with our resolution for our gprMax simulations. At the same time, the different range resolution (4.3 m for the measured RES data and 2.1 m for our simulated RES data) influences the total volume of point reflectors illuminated at one time. Therefore, we limit our interpretations to a large extent to comparing the simulation results with each other rather than directly comparing the measured with the simulated data.

In addition, gprMax simulates a single pulse as a source instead of the narrowband 10-μs chirp used in the field data. Both circumstances lead to additional limitations in the accuracy and extent of the conclusions that can be drawn by comparing the measured and modeled data. In reality, englacial attenuation and the longer travel path lead to an overall decrease in signal strength and a wavefront that is more planar than the one in our simulations. The gprMax version used here cannot yet model planar waves but is planned for future versions. Nonetheless, since we analyze and compare the relative values of the backscatter between the HBZ onset, within the HBZ, and between the HBZ and the ice base, we can largely neglect the energy losses due to the englacial attenuation.

Another simplification in our model is the representation of the ice–bed interface, which is represented as a smooth, horizontal transition. The measured radar signatures of real subglacial environments contain, in addition to the change in dielectric properties, other components that affect the reflected radar signal. In particular, the roughness at the bed [67], the slope relative to the receiver, and the influence of side reflections [68] are not considered here. However, some of the effects acting on the backscatter of the subglacial environment can be partly disregarded, especially if the reflection at the base of the HBZ is stronger than at its onset. This would most likely still support a stronger change in dielectric properties at the ice–bed transition than at the HBZ onset since geometric characteristics such as bed slope and roughness would reduce the reflected energy rather than increase it. It is also expected that side reflections are usually weaker than reflections from nadir.

VI. Conclusion

This article presents a conceptual study that focuses on systematically constraining the structure characteristics of basal ice units in the East Antarctic Ice Sheet. HBZs were classified via particular reflection signatures in the near-base environment in the Jutulstraumen drainage basin at the onset of the Jutulstraumen Ice Stream. Using numerical modeling of radar waves with gprMax, we defined scenarios with different material compositions that may constitute HBZs and create the typical radar reflection signature. In our simulations, we have focused on comparing the transition from echo-free (or low-backscatter) ice to ice with slightly different dielectric properties and HBZs composed of point reflectors

with the measured field radar data. For the HBZs composed of point reflectors, we also studied the effect of grain size and particle concentration in combination with different dielectric properties on the radar signature.

Our simulations are a simplification of radar wave propagation in complex subsurface environments. They indicate that the HBZs in the Jutulstraumen drainage basin may consist of a wide range of particle concentrations of entrained sediment with low dielectric properties or particles with higher dielectric properties at a lower concentration. Furthermore, our simulations provide indications that it is rather unlikely that the HBZs consist of temperate ice. Still, interpreting the simulated radar signatures should be treated with caution. The reflection patterns of embedded water droplets and sediment with high dielectric properties are partly very similar and thus ambiguous but represent completely different basal conditions. In general, we see significant potential in forward simulations, like with gprMax, to help decipher the composition and characteristics of Antarctic and Greenland ice.

ACKNOWLEDGMENT

The authors thank the Kenn Borek crew as well as Martin Gehrmann and Sebastian Spelz of AWI's technical staff of the research aircraft Polar 6. John Paden (University of Kansas) assisted remotely during the field campaign. They want to thank Tobias Binder for the implementation of the AWI UWB radar as well as an acquisition backup system. Logistical support in Antarctica was provided at Troll Station (Norway), Novolazarewskaja-Station (Russia), Kohnen Station (Germany), and Neumayer Station III (Germany).

The EM wave propagation software gprMax (https://www.gprmax.com) is open-source and freely available under https://github.com/gprmax/gprMax. The simulation outputs as well as gprMax input files to reproduce the results are available at the Electronic Research Data Archive (ERDA) of the University of Copenhagen: http://doi.org/10.17894/ucph.9316566f-37ef-4618-a228-ebee347ae0a4. This article was produced by the IEEE Publication Technology Group. They are in Piscataway, NJ.

REFERENCES

[1] G. D. Q. Robin, S. Evans, and J. T. Bailey, "Interpretation of radio echo sounding in polar ice sheets," *Phil. Trans. Roy. Soc. London. Ser. A, Math. Phys. Sci.*, vol. 265, no. 1166, pp. 437–505, 1969, doi: 10.1098/rsta.1969.0063.

[2] C. R. Bentley, N. Lord, and C. Liu, "Radar reflections reveal a wet bed beneath stagnant ice stream c and a frozen bed beneath ridge BC, West Antarctica," *J. Glaciol.*, vol. 44, no. 146, pp. 149–156, 1998, doi: 10.3189/S0022143000002434.

[3] J. A. Bodart, R. G. Bingham, D. W. Ashmore, N. B. Karlsson, A. S. Hein, and D. G. Vaughan, "Age-depth stratigraphy of pine island glacier inferred from airborne radar and ice-core chronology," *J. Geophys. Res., Earth Surf.*, vol. 126, no. 4, Apr. 2021, doi: 10.1029/2020jf005927.

[4] S. Franke et al., "Complex basal conditions and their influence on ice flow at the onset of the northeast Greenland ice stream," *J. Geophys. Res., Earth Surf.*, vol. 126, no. 3, Mar. 2021, doi: 10.1029/2020jf005689.

[5] R. Drews et al., "Layer disturbances and the radio-echo free zone in ice sheets," *Cryosphere*, vol. 3, no. 2, pp. 195–203, Aug. 2009, doi: 10.5194/tc-3-195-2009.

[6] R. E. Bell et al., "Widespread persistent thickening of the east Antarctic ice sheet by freezing from the base," *Science*, vol. 331, no. 6024, pp. 1592–1595, Mar. 2011, doi: 10.1126/science.1200109.

[7] R. E. Bell et al., "Deformation, warming and softening of Greenland's ice by refreezing meltwater," *Nature Geosci.*, vol. 7, no. 7, pp. 497–502, Jul. 2014, doi: 10.1038/ngeo2179.

[8] T. T. Creyts et al., "Freezing of ridges and water networks preserves the Gamburtsev Subglacial Mountains for millions of years," *Geophys. Res. Lett.*, vol. 41, no. 22, pp. 8114–8122, Nov. 2014, doi: 10.1002/2014gl061491.

[9] G. J.-M.-C. Leysinger Vieli, C. Martín, R. C. A. Hindmarsh, and M. P. Lüthi, "Basal freeze-on generates complex ice-sheet stratigraphy," *Nature Commun.*, vol. 9, no. 1, p. 4669, Nov. 2018, doi: 10.1038/s41467-018-07083-3.

[10] P. D. Bons et al., "Converging flow and anisotropy cause large-scale folding in Greenland's ice sheet," *Nature Commun.*, vol. 7, no. 1, p. 11427, Apr. 2016, doi: 10.1038/ncomms11427.

[11] N. Ross, H. Corr, and M. Siegert, "Large-scale englacial folding and deep-ice stratigraphy within the west Antarctic ice sheet," *Cryosphere*, vol. 14, no. 6, pp. 2103–2114, Jun. 2020, doi: 10.5194/tc-14-2103-2020.

[12] S. Franke et al., "Holocene ice-stream shutdown and drainage basin reconfiguration in northeast Greenland," *Nature Geosci.*, vol. 15, no. 12, pp. 995–1001, Dec. 2022, doi: 10.1038/s41561-022-01082-2.

[13] K. Winter et al., "Radar-detected englacial debris in the west Antarctic ice sheet," *Geophys. Res. Lett.*, vol. 46, nos. 17–18, pp. 10454–10462, Sep. 2019, doi: 10.1029/2019gl084012.

[14] R. Pettersson, "Frequency dependence of scattering from the cold-temperate transition surface in a polythermal glacier," *Radio Sci.*, vol. 40, no. 3, pp. 1–7, Jun. 2005, doi: 10.1029/2004RS003090.

[15] C. Schannwell, T. Murray, B. Kulessa, A. Gusmeroli, A. Saintenoy, and P. Jansson, "An automatic approach to delineate the cold–temperate transition surface with ground-penetrating radar on polythermal glaciers," *Ann. Glaciol.*, vol. 55, no. 67, pp. 89–96, 2014, doi: 10.3189/2014AoG67A102.

[16] J. H. McBride et al., "Radar scattering in an alpine glacier: Evidence of seasonal development of temperate ice beneath ogives," *Geosphere*, vol. 8, no. 5, pp. 1054–1077, 2012, doi: 10.1130/ges00804.1.

[17] H. Sevestre, D. I. Benn, N. R. J. Hulton, and K. Bælum, "Thermal structure of svalbard glaciers and implications for thermal switch models of glacier surging," *J. Geophys. Res., Earth Surf.*, vol. 120, no. 10, pp. 2220–2236, Oct. 2015, doi: 10.1002/2015jf003517.

[18] D. A. Lilien et al., "Brief communication: New radar constraints support presence of ice older than 1.5 Myr at little dome C," *Cryosphere*, vol. 15, no. 4, pp. 1881–1888, Apr. 2021, doi: 10.5194/tc-15-1881-2021.

[19] P. Christoffersen, S. Tulaczyk, and A. Behar, "Basal ice sequences in Antarctic ice stream: Exposure of past hydrologic conditions and a principal mode of sediment transfer," *J. Geophys. Res.*, vol. 115, no. F3, pp. 1–12, 2010, doi: 10.1029/2009jf001430.

[20] N. Neckel, S. Franke, V. Helm, R. Drews, and D. Jansen, "Evidence of cascading subglacial water flow at Jutulstraumen Glacier (Antarctica) derived from Sentinel-1 and ICESat-2 measurements," *Geophys. Res. Lett.*, vol. 48, no. 20, Oct. 2021, Art. no. e2021GL094472, doi: 10.1029/2021gl094472.

[21] L. K. Zoet et al., "The effects of entrained debris on the basal sliding stability of a glacier," *J. Geophys. Res., Earth Surf.*, vol. 118, no. 2, pp. 656–666, Jun. 2013, doi: 10.1002/jgrf.20052.

[22] E. J. Dawson, D. M. Schroeder, W. Chu, E. Mantelli, and H. Seroussi, "Ice mass loss sensitivity to the Antarctic ice sheet basal thermal state," *Nature Commun.*, vol. 13, no. 1, p. 4957, Sep. 2022, doi: 10.1038/s41467-022-32632-2.

[23] K. H. Kjær et al., "A large impact Crater beneath Hiawatha Glacier in Northwest Greenland," *Sci. Adv.*, vol. 4, no. 11, Nov. 2018, Art. no. eaar8173, doi: 10.1126/sciadv.aar8173.

[24] W. D. Miners, A. Hildebrand, S. Gerland, N. Blindow, D. Steinhage, and E. W. Wolff, "Forward modeling of the internal layers in radio echo sounding using electrical and density measurements from ice cores," *J. Phys. Chem. B*, vol. 101, no. 32, pp. 6201–6204, 1997, doi: 10.1021/jp963218+.

[25] W. D. Miners, E. W. Wolff, J. C. Moore, R. Jacobel, and L. Hempel, "Modeling the radio echo reflections inside the ice sheet at summit, Greenland," *J. Geophys. Res.*, vol. 107, no. B8, p. 6, 2002, doi: 10.1029/2001jb000535.

[26] O. Eisen, F. Wilhelms, U. Nixdorf, and H. Miller, "Identifying isochrones in GPR profiles from DEP-based forward modeling," *Ann. Glaciol.*, vol. 37, pp. 344–350, Jan. 2003, doi: 10.3189/172756403781816068.

[27] O. Eisen, F. Wilhelms, U. Nixdorf, and H. Miller, "Revealing the nature of radar reflections in ice: DEP-based FDTD forward modeling," *Geophys. Res. Lett.*, vol. 30, no. 5, 2003, doi: 10.1029/2002gl016403.

[28] S. Mojtabavi et al., "Origin of englacial stratigraphy at three deep ice core sites of the Greenland ice sheet by synthetic radar modelling," *J. Glaciol.*, vol. 68, no. 270, pp. 799–811, Aug. 2022, doi: 10.1017/jog.2021.137.

[29] C. Warren, A. Giannopoulos, and I. Giannakis, "GprMax: Open source software to simulate electromagnetic wave propagation for ground penetrating radar," *Comput. Phys. Commun.*, vol. 209, pp. 163–170, Dec. 2016, doi: 10.1016/j.cpc.2016.08.020.

[30] A. Giannopoulos, "Modelling ground penetrating radar by GprMax," *Construct. Building Mater.*, vol. 19, no. 10, pp. 755–762, Dec. 2005, doi: 10.1016/j.conbuildmat.2005.06.007.

[31] G. Church, M. Grab, C. Schmelzbach, A. Bauder, and H. Maurer, "Monitoring the seasonal changes of an englacial conduit network using repeated ground-penetrating radar measurements," *Cryosphere*, vol. 14, no. 10, pp. 3269–3286, Oct. 2020, doi: 10.5194/tc-14-3269-2020.

[32] K. Sokolov, L. Fedorova, and M. Fedorov, "Prospecting and evaluation of underground massive ice by ground-penetrating radar," *Geosciences*, vol. 10, no. 7, p. 274, Jul. 2020, doi: 10.3390/geosciences10070274.

[33] T. R. Hillebrand, H. Conway, M. Koutnik, C. Martín, J. Paden, and J. P. Winberry, "Radio-echo sounding and waveform modeling reveal abundant marine ice in former rifts and basal crevasses within Crary Ice Rise, Antarctica," *J. Glaciol.*, vol. 67, no. 264, pp. 641–652, Aug. 2021, doi: 10.1017/jog.2021.17.

[34] S. Franke et al., "Preserved landscapes underneath the Antarctic ice sheet reveal the geomorphological history of Jutulstraumen basin," *Earth Surf. Processes Landforms*, vol. 46, no. 13, pp. 2728–2745, Oct. 2021, doi: 10.1002/esp.5203.

[35] C. Wesche, D. Steinhage, and U. Nixdorf, "Polar aircraft polar5 and polar6 operated by the alfred Wegener institute," *J. Large-Scale Res. Facilities*, vol. 2, p. 87, Sep. 2016, doi: 10.17815/jlsrf-2-153.

[36] F. Rodriguez-Morales et al., "Advanced multifrequency radar instrumentation for polar research," *IEEE Trans. Geosci. Remote Sens.*, vol. 52, no. 5, pp. 2824–2842, May 2014, doi: 10.1109/TGRS.2013.2266415.

[37] R. Hale et al., "Multi-channel ultra-wideband radar sounder and imager," in *Proc. IEEE Int. Geosci. Remote Sens. Symp. (IGARSS)*, Nov. 2016, pp. 2112–2115, doi: 10.1109/IGARSS.2016.7729545.

[38] S. Franke et al., "Airborne ultra-wideband radar sounding over the shear margins and along flow lines at the onset region of the northeast Greenland ice stream," *Earth Syst. Sci. Data*, vol. 14, no. 2, pp. 763–779, Feb. 2022, doi: 10.5194/essd-14-763-2022.

[39] M. Morlighem et al., "Deep glacial troughs and stabilizing ridges unveiled beneath the margins of the Antarctic ice sheet," *Nature Geosci.*, vol. 13, no. 2, pp. 132–137, Feb. 2020, doi: 10.1038/s41561-019-0510-8.

[40] CReSIS, "cresis-toolbox (Version 3.0.1) [computer software]," Centre Remote Sens. Integr. Syst. (CReSIS), Univ. Kansas, Lawrence, KS, USA, Tech. Rep., 2021, doi: 10.5281/zenodo.5683959.

[41] C. Leuschen, S. Gogineni, and D. Tammana, "SAR processing of radar echo sounder data," in *Proc. IEEE Int. Geosci. Remote Sens. Symp. (IGARSS), Taking Pulse Planet, Role Remote Sens. Manag. Environ.*, Jun. 2000, pp. 2570–2572, doi: 10.1109/IGARSS.2000.859643.

[42] J.-O. Näslund, "Landscape development in western and central Dronning Maud Land, east Antarctica," *Antarctic Sci.*, vol. 13, no. 3, pp. 302–311, Sep. 2001, doi: 10.1017/S0954102001000438.

[43] T. Wrona, M. J. Wolovick, F. Ferraccioli, H. Corr, T. Jordan, and M. J. Siegert, "Position and variability of complex structures in the central east Antarctic ice sheet," *Geological Soc., London, Special Publications*, vol. 461, no. 1, pp. 113–129, Jan. 2018, doi: 10.1144/sp461.12.

[44] A. Taflove and S. C. Hagness, *Computational Electrodynamics: The Finite Difference Time-Domain Method*, 3rd ed. Norwood, MA, USA: Artech House, 2005.

[45] K. Yee, "Numerical solution of initial boundary value problems involving Maxwell's equations in isotropic media," *IEEE Trans. Antennas Propag.*, vol. AP-14, no. 3, pp. 302–307, May 1966, doi: 10.1109/TAP.1966.1138693.

[46] O. Eisen, F. Wilhelms, D. Steinhage, and J. Schwander, "Improved method to determine radio-echo sounding reflector depths from ice-core profiles of permittivity and conductivity," *J. Glaciol.*, vol. 52, no. 177, pp. 299–310, 2006, doi: 10.3189/172756506781828674.

[47] A. Winter et al., "Comparison of measurements from different radio-echo sounding systems and synchronization with the ice core at dome C, Antarctica," *Cryosphere*, vol. 11, no. 1, pp. 653–668, Mar. 2017, doi: 10.5194/tc-11-653-2017.

[48] C. Warren et al., "A CUDA-based GPU engine for gprMax: Open source FDTD electromagnetic simulation software," *Comput. Phys. Commun.*, vol. 237, pp. 208–218, Apr. 2019, doi: 10.1016/j.cpc.2018.11.007.

[49] A. Giannopoulos, "Unsplit implementation of higher order PMLs," *IEEE Trans. Antennas Propag.*, vol. 60, no. 3, pp. 1479–1485, Mar. 2012, doi: 10.1109/TAP.2011.2180344.

[50] K. S. Kunz and R. J. Luebbers, *The Finite Difference Time Domain Method for Electromagnetics*. Boca Raton, FL, USA: CRC Press 1993.

[51] O. Eisen, I. Hamann, S. Kipfstuhl, D. Steinhage, and F. Wilhelms, "Direct evidence for continuous radar reflector originating from changes in crystal-orientation fabric," *Cryosphere*, vol. 1, no. 1, pp. 1–10, Oct. 2007, doi: 10.5194/tc-1-1-2007.

[52] P. Bohleber, N. Wagner, and O. Eisen, "Permittivity of ice at radio frequencies: Part II. Artificial and natural polycrystalline ice," *Cold Regions Sci. Technol.*, vols. 83–84, pp. 13–19, Dec. 2012, doi: 10.1016/j.coldregions.2012.05.010.

[53] K. Christianson et al., "Basal conditions at the grounding zone of Whillans ice stream, west antarctica, from ic-penetrating radar," *J. Geophys. Res., Earth Surf.*, vol. 121, no. 11, pp. 1954–1983, Nov. 2016, doi: 10.1002/2015jf003806.

[54] J. L. Davis and A. P. Annan, "Ground-penetrating radar for high-resolution mapping of soil and rock stratigraphy1," *Geophys. Prospecting*, vol. 37, no. 5, pp. 531–551, Jul. 1989, doi: 10.1111/j.1365-2478.1989.tb02221.x.

[55] S. M. Tulaczyk and N. T. Foley, "The role of electrical conductivity in radar wave reflection from glacier beds," *Cryosphere*, vol. 14, no. 12, pp. 4495–4506, Dec. 2020, doi: 10.5194/tc-14-4495-2020.

[56] B. C. Christner et al., "A microbial ecosystem beneath the west Antarctic ice sheet," *Nature*, vol. 512, no. 7514, pp. 310–313, Aug. 2014, doi: 10.1038/nature13667.

[57] A. J. Gow, S. Epstein, and W. Sheehy, "On the origin of stratified debris in ice cores from the bottom of the Antarctic ice sheet," *J. Glaciol.*, vol. 23, no. 89, pp. 185–192, 1979, doi: 10.3189/s0022143000029828.

[58] J. L. Tison, J. R. Petit, J. M. Barnola, and W. C. Mahaney, "Debris entrainment at the ice-bedrock interface in sub-freezing temperature conditions (Terre Adélie, Antarctica)," *J. Glaciol.*, vol. 39, no. 132, pp. 303–315, 1993, doi: 10.3189/s0022143000015963.

[59] P. Christoffersen, S. Tulaczyk, F. D. Carsey, and A. E. Behar, "A quantitative framework for interpretation of basal ice facies formed by ice accretion over subglacial sediment," *J. Geophys. Res.*, vol. 111, no. F1, pp. 1–12, 2006, doi: 10.1029/2005jf000363.

[60] T. Murray, G. W. Stuart, M. Fry, N. H. Gamble, and M. D. Crabtree, "Englacial water distribution in a temperate glacier from surface and borehole radar velocity analysis," *J. Glaciol.*, vol. 46, no. 154, pp. 389–398, 2000, doi: 10.3189/172756500781833188.

[61] R. Pettersson, P. Jansson, and H. Blatter, "Spatial variability in water content at the cold-temperate transition surface of the polythermal Storglaciären, Sweden," *J. Geophys. Res., Earth Surf.*, vol. 109, no. F2, pp. 1–12, Jun. 2004, doi: 10.1029/2003JF000110.

[62] F. Wilhelms, J. Kipfstuhl, H. Miller, K. Heinloth, and J. Firestone, "Precise dielectric profiling of ice cores: A new device with improved guarding and its theory," *J. Glaciol.*, vol. 44, no. 146, pp. 171–174, 1998, doi: 10.3189/S002214300000246X.

[63] M. J. Wolovick, J. C. Moore, and L. Zhao, "Joint inversion for surface accumulation rate and geothermal heat flow from ice-penetrating radar observations at dome A, East Antarctica. Part I: Model description, data constraints, and inversion results," *J. Geophys. Res., Earth Surf.*, vol. 126, no. 5, May 2021, Art. no. e2020JF005936, doi: 10.1029/2020jf005937.

[64] M. J. Wolovick, J. C. Moore, and L. Zhao, "Joint inversion for surface accumulation rate and geothermal heat flow from ice-penetrating radar observations at dome A, East Antarctica. Part II: Ice sheet state and geophysical analysis," *J. Geophys. Res., Earth Surf.*, vol. 126, no. 5, May 2021, Art. no. e2020JF005936, doi: 10.1029/2020jf005936.

[65] P. G. Knight, "Two-facies interpretation of the basal layer of the Greenland ice sheet contributes to a unified model of basal ice formation," *Geology*, vol. 22, no. 11, pp. 971–974, 1994, doi: 10.1130/0091-7613(1994)022<0971:TFIOTB>2.3.CO;2.

[66] B. P. Lipovsky et al., "Glacier sliding, seismicity and sediment entrainment," *Ann. Glaciol.*, vol. 60, no. 79, pp. 182–192, Sep. 2019, doi: 10.1017/aog.2019.24.

[67] T. M. Jordan et al., "Self-affine subglacial roughness: Consequences for radar scattering and basal water discrimination in northern Greenland," *Cryosphere*, vol. 11, no. 3, pp. 1247–1264, May 2017, doi: 10.5194/tc-11-1247-2017.

[68] S. Franke et al., "Bed topography and subglacial landforms in the onset region of the northeast Greenland ice stream," *Ann. Glaciol.*, vol. 61, no. 81, pp. 143–153, Apr. 2020, doi: 10.1017/aog.2020.12.

Steven Franke received the B.Sc. degree from Freie Universität Berlin, Berlin, Germany, in 2013, the M.Sc. degree from Københavns Universitet, Copenhagen, Denmark, in 2015, and the Ph.D. degree from the Alfred Wegener Institute, Bremerhaven, Germany, and Universität Bremen, Bremen, Germany, in 2021, all in geosciences.

Between 2015 and 2017, he overwintered at the German Antarctic Research Station Neumayer III, Antarctica, as a Geophysicist. After the Ph.D. degree, he worked on radioglaciological projects at the Alfred Wegener Institute and the Centre for Ice and Climate, University of Copenhagen. In 2023, he joined the Geoscience Department, University of Tübingen (funded by the DFG Walter Benjamin Programme), Tübingen, Germany, studying englacial and basal radar reflection signals in the East Antarctic ice sheet.

Tamara Gerber received the B.Sc. and M.Sc. degrees in geophysics from the Swiss Federal Institute of Technology (ETH), Zürich, Switzerland, in 2016 and 2018, respectively, and the Ph.D. degree from the University of Copenhagen, Copenhagen, Denmark, in 2022, with a strong focus on interpreting ice-flow dynamics in the Greenland ice sheet with radar methods and gprMax modeling.

She has been holding a post-doctoral position with the Section for Physics of Ice, Climate and Earth, University of Copenhagen, concentrating on radar measurements and their analysis in terms of ice dynamics and stratigraphy.

Craig Warren received the B.Eng. degree in electrical and mechanical engineering and the Ph.D. degree in engineering from The University of Edinburgh, Edinburgh, U.K., in 2003 and 2009, respectively.

He is currently an Assistant Professor of civil engineering with the Department of Mechanical and Construction Engineering, Northumbria University, Newcastle, U.K. He carries out fundamental and applied research on sensing technologies for infrastructure and geophysical applications. He has a specific interest in the numerical modeling and optimization of electromagnetic sensing systems, such as ground penetrating radar (GPR). He is a Lead Developer of open-source software gprMax, which simulates electromagnetic wave propagation and is the most widely used software for modeling GPR. He is also active in the fields of engineering education and technology-enhanced learning.

Dr. Warren is a Chartered Engineer (CEng), a fellow of The Higher Education Academy (FHEA), U.K., and a member of the Institution of Mechanical Engineers (IMechE), U.K., the Institution of Engineering Technology (IET), U.K., the European Association of Geoscientists and Engineers (EAGE), The Netherlands, and the Society of Exploration Geophysicists (SEG), USA. He was the Co-Chair for the 9th and 10th International Workshops on Advanced Ground Penetrating Radar, Edinburgh, in 2017 and 2019, and The Hague, The Netherlands.

Daniela Jansen received the Ph.D. degree in geosciences from the University of Bremen, Bremen, Germany, in 2009.

Between 2008 and 2012, she held a post-doctoral position with Swansea University, Swansea, U.K., where she was involved in glaciology on the Larsen C breakup, ice shelf modeling, and analysis of ground-penetrating radar data. She is currently a Senior Scientist at the Alfred Wegener Institute, Bremerhaven, Germany, works on various topics related to ice sheets and ice shelves. Methodologically, she has worked in many areas of glaciology and gained expertise in modeling, remote sensing techniques, field measurements, and ice core analysis. Her research interests include radar stratigraphy of ice sheets and its relation to rheological properties and microdynamic processes in Greenland and Antarctica.

Olaf Eisen received the Diploma degree in geophysics from the Technical University of Karlsruhe, Karlsruhe, Germany, in 1999, where he performed research on the contribution of sea ice to the ocean–ice–atmosphere interaction, and the Ph.D. degree from the University of Bremen, Bremen, Germany, in 2003, worked on the nature of electromagnetic reflection in ice.

Since 1999, he has been with the Alfred-Wegener Institute (AWI), Helmholtz Center for Polar and Marine Research, Bremerhaven, Germany. During stays at the University of Alaska, Fairbanks, AK, USA, in 2000, and ETH Zürich, Zürich, Switzerland, from 2005 to 2006, he conducted research on the interaction of climate and ice dynamics. From 2008 to 2013, he led the Emmy Noether Young Investigators Group, University of Heidelberg, Heidelberg, Germany, and AWI, applying geophysical methods on ice sheets and glaciers, with habilitation, in 2010, and Associated Professorship, in 2013. Since 2014, he has been a Joint Professor for Glaciology with AWI, focusing on the application of geophysical methods in cryospheric research.

Dorthe Dahl-Jensen received the M.Sc. and Ph.D. degrees in geophysics from the University of Copenhagen, Copenhagen, Demark, in 1984, and 1988, respectively.

She is currently a Professor with the Niels Bohr Institute, University of Copenhagen, and the Canada Excellence Research Chair with the Centre for Earth Observation Science, University of Manitoba, Winnipeg, MB, Canada. Her major scientific achievements have been in leading ice core drilling and subsequent analysis of ice core data in conjunction with models to determine past climate and how it affected the Greenland ice sheet. She has led several international deep drilling projects, such as NGRIP, NEEM, and EGRIP. In addition, she has led large research projects funded by grants from the Danish National Research Foundation (DNRF), European Research Council (ERC), EU FP7, Villum Investigator, and Canada Excellence Research Chair. The research has led to numerous achievements and here are some highlights to illustrate how the past illuminates potential future abrupt climate changes. During the Last Interglacial where Greenland temperatures were 5 °C warmer than the present, the Greenland ice sheet thinned and contributed to the global sea level rise by about 2 m. Dated Greenland ice cores through the past 2000 years show the impact on the atmosphere from human activities, such as forest burning and industrialization, and from volcanic eruptions producing aerosols that cool the Earth surface for about ten summers following the event. Synchronized ice cores from Greenland and Antarctica show 25 very abrupt climate changes during the last glacial and modeling shows that the events represent internal movement of energy through ocean and atmosphere between the Northern and Southern hemispheres. The research is very well cited, and five others and she from her research group are Thomson Reuters highly cited researchers.